PERGAMON

International Journal of Solids and Structures 37 (2000) 5529–5559

INTERNATIONAL JOURNAL OF SOLIDS and STRUCTURES

www.elsevier.com/locate/ijsolstr

Multi-resolution multi-scale topology optimization — a new paradigm

Yoon Young Kim*, Gil Ho Yoon

School of Mechanical and Aerospace Engineering, Institute of Advanced Machinery Design, Seoul National University, Shinlim-Dong, San 56-1, Kwanak-Gu, Seoul 151-742, South Korea

Received 24 June 1999; in revised form 28 August 1999

Abstract

The purpose of this work is to present a new-concept multi-resolution multi-scale topology optimization. The key idea of the present strategy is that design optimization should be performed progressively from low to high resolution, not at a single resolution level. To achieve the multi-resolution strategy, design optimization is formulated in a wavelet-based variable space, not in a direct density variable space. The major advantages of the multi-resolution design optimization include: (1) topologically simple and close-to-the-global-optimum structures may be obtained without any explicit constraint, and (2) the convergence is not sensitive to mathematical programming methods. For the efficient numerical implementation of the multi-resolution approach, the side constraints imposed on the direct density variables are removed by mapping the density variables into intermediate variables. These intermediate variables are then wavelet-transformed to new design variables. It is addressed that the present multi-resolution topology optimization can resolve major numerical instability problems such as mesh-dependencies and local minima. The usefulness of the multi-scale nature of the wavelets in the present multi-resolution multi-scale optimization formulation is also discussed.

Keywords: Multi-resolution; Multi-scale; Topology optimization; Wavelet

1. Introduction

Topology optimization has become an important design method and been applied to many practical problems. Extensive references on topology optimization can be found in Bendsøe and Kikuchi (1988) and Bendsøe (1995). Hassani and Hinton (1998a, 1998b, 1998c) also give a recent review on topology optimization and related subjects. Sigmund and Petersson (1998) gave an excellent review on several

* Corresponding author. Tel.: +82-2-880-7154; fax: +82-2-883-1513.
E-mail address: yykim@snu.ac.kr (Y.Y. Kim).

0020-7683/00/$ - see front matter
PII: S0020-7683(99)00251-6

available techniques dealing with numerical instability problems including checkerboards, mesh-dependencies, and local minima. No attempt is made here to refer to all the previous publications on the subject of topology optimization; see the papers cited above.

In order to develop an efficient topology optimization method, a new attempt based on wavelets has been recently coined by one of the present authors. Kim and Choi (1998) transformed direct density variables into new variables using a wavelet transform.[1] The idea was that topology optimization can be carried out more effectively in the wavelet transformed space than in the direct density space since wavelets can detect very efficiently the edges and corners of an image. They applied the wavelet-based method to section topology optimization problems formulated by Kim and Kim (2000) and reported that the solution convergence rate can be substantially improved. More numerical results can be found in Choi (1999). Kim and Kim (1999) have also indicated that the design optimization in the wavelet space can control effectively checkerboard patterns, typical in the low-order finite element analysis. Poulsen (1999) also discusses the possibility of using wavelets for attacking numerical instabilities such as checkerboards. However, none of these works has suggested that wavelets may be useful for multi-resolution topology optimization.

In this work, we formulate multi-resolution multi-scale topology optimization using wavelet transforms. This approach differs from any other existing approach in that the latter has no notion of resolution. The essence of the multi-resolution optimization is to start optimization at a low-resolution level and move to the next higher-resolution level until the highest-resolution level is reached. In this multi-resolution optimization strategy, the optimized structural topology at a certain resolution level can be used as an initial guess for optimization at the next level. The progression from a coarse to a fine resolution level is achieved in a using wavelet-transformed variable space, not in a direct density variable space. The wavelet-based design variables are multi-scaled, ranging from the longest scale to the scale proportional to a resolution level. The multi-scale nature of wavelets allows the systematic and efficient implementation of multi-resolution optimization.

The advantages of the multi-resolution design optimization in the wavelet spaces, which we have found so far, are the followings. (1) Topologically simple structures, which are close to the global optima, may be obtained when an appropriate wavelet is employed; (2) the solution convergence appears insensitive to mathematical programming methods; (3) the rate of the solution convergence can be greatly enhanced if optimization is carried out in the wavelet space. Obtaining topologically simple and close-to-the-global-optimum structures is, in principle, equivalent to obtaining mesh- independent optimized structures. There are several mesh-independent approaches (Harber et al., 1996; Sigmund and Petersson, 1998; Sigmund, 1994, 1997), but these approaches use either explicit constraints or filtering schemes. However, the present approach yields topologically simple and close-to-the-global-optimum structures without any explicit constraint.

For the efficient numerical implementation of the present multi-resolution optimization strategy, we eliminate the side constraints imposed on the density variables by introducing intermediate variables. To this end, we propose to use the Sigmoid function, an S-shaped function, as the mapping function of the direct density variables to the intermediate variables. The intermediate variables are then transformed to new design variables by a wavelet transform. If the wavelet transform were applied to the original density variables, the side constraints would cause undesirable numerical complexity and thus designing in the wavelet-space would not be very attractive. If the support of a wavelet is long, the numerical complexity becomes more serious.

We consider several numerical examples including the classical Michell benchmark in order to show

[1] For wavelet theories and applications, one may refer to Chui (1992), Daubechies (1992), Vetterli and Kovacevic (1995), Strang and Nguyen (1996) and Mallat (1998).

the validity of the present idea of multi-resolution topology optimization. The material model employed is an artificial material model (see, e.g., Hassani and Hinton, 1998b). To solve topology optimization problems, non-linear mathematical programming methods are utilized. Specifically, the methods of feasible and modified feasible directions are employed (see, Vanderplaats, 1984a). With the numerical examples, the effects of optimizers, mesh size, and the type of wavelets are also examined.

2. Topology optimization

This section lists basic equations needed in topology optimization. A compliance minimization is considered here as a typical structural optimization problem:

Minimization of $L(\boldsymbol{\rho})$:

$$L(\boldsymbol{\rho}) = \boldsymbol{U}^{\mathrm{T}}(\boldsymbol{\rho})\boldsymbol{F} = \boldsymbol{U}^{\mathrm{T}}(\boldsymbol{\rho})\boldsymbol{K}(\boldsymbol{\rho})\boldsymbol{U}(\boldsymbol{\rho}) \tag{1}$$

Subjected to

$$H(\boldsymbol{\rho}) = \sum_{e=1}^{N_e \times M_e} \int_{\Omega_e} \rho_e \, \mathrm{d}\Omega - M_0 \leq 0 \tag{2}$$

The optimization problem set up by Eqs. (1) and (2) is based on a finite element model. No constraint such as the perimeter constraint (Harber et al., 1996) is considered here.

The external force is represented by a nodal force array $\boldsymbol{F}$ and the displacement field is expressed by a nodal displacement array $\boldsymbol{U}$. The specified mass is denoted by M_0 and Ω_e represents the region occupied by a finite element. Optimization problems only in a two-dimensional rectangular region are considered in this work without the loss of generality. The numbers of elements in the horizontal and vertical directions are denoted by N_e and M_e, respectively. The array $\boldsymbol{\rho}$ is used to denote:

$$\boldsymbol{\rho} = \{\rho_e\}^{\mathrm{T}} \quad (e = 1, 2, \ldots, N_e \times M_e) \tag{3}$$

The stiffness matrix $\boldsymbol{K}(\boldsymbol{\rho})$ in Eq. (1) can be expressed as:

$$\boldsymbol{K}(\boldsymbol{\rho}) = \sum_{e=1}^{N_e \times M_e} \boldsymbol{K}_e(\rho_e) = \sum_{e=1}^{N_e \times M_e} \int_{\Omega_e} \boldsymbol{B}_e^{\mathrm{T}} \boldsymbol{D}(\rho_e) \boldsymbol{B}_e \, \mathrm{d}\Omega \tag{4}$$

where $\boldsymbol{B}_e$ is the strain interpolation matrix. The stress–strain relation for an isotropic material in a plane stress state, represented by $\boldsymbol{D}_e(\rho_e)$, is:

$$\boldsymbol{D}(\rho_e) = \frac{E(\rho_e)}{1-\nu^2} \begin{bmatrix} 1 & \nu & 0 \\ \nu & 1 & 0 \\ 0 & 0 & \dfrac{1-\nu}{2} \end{bmatrix} \tag{5}$$

Poisson's ratio ν is assumed to be independent of ρ_e and only Young's modulus E is penalized as (see, e.g. Hassani and Hinton, 1998b):

$$E(\rho_e) = E_0 \rho_e^n \quad (n = 2) \tag{6}$$

In Eq. (6), Young's modulus of the given material is denoted by E_0. In topology optimization, ρ_e is used as the design variable and subjected to the following side constraint:

$$\varepsilon \le \rho_e \le 1 \quad (0 < \varepsilon \ll 1) \tag{7}$$

The sensitivity of the object function $L(\boldsymbol{\rho})$ and the constraint $H(\boldsymbol{\rho})$ can be easily found as:

$$\frac{\partial L}{\partial \rho_e} = -\boldsymbol{U}_e^{\mathrm{T}} \frac{\partial \boldsymbol{K}_e}{\partial \rho_e} \boldsymbol{U}_e = -\frac{n}{\rho_e} \boldsymbol{U}_e^{\mathrm{T}} \boldsymbol{K}_e \boldsymbol{U}_e = -\frac{2n}{\rho_e} \times (\text{element strain energy}) \tag{8}$$

and

$$\frac{\partial H}{\partial \rho_e} = \int_{\Omega_e} \mathrm{d}\Omega \tag{9}$$

3. Wavelet trasform

It is crucial to use wavelet-based design variables in achieving multi-resolution multi-scale design optimization. This is because multi-resolution approximation can be easily realized in the framework of wavelets. In addition, most wavelets represent functional differences very efficiently. As a result, the boundary of a topologically optimized structure can be captured very effectively when design optimization is carried out in the wavelet-based variable space (Kim and Choi, 1998).

In this section, we present the multi-resolution approximation of $L^2(R)$ with a sequence of subspaces $\{V^j\}_{j\in Z}$ (R: set of real numbers, Z: set of integers). Referring to Mallat (1998), the following six statements formulate the multi-resolution of $L^2(R)$:

$$\forall j, k \in Z, \quad f(t) \in V^j \Leftrightarrow f(t - 2^j k) \in V^j \tag{10a}$$

$$\forall j \in Z, \quad V^{j+1} \subset V^j \tag{10b}$$

$$\forall j \in Z, \quad f(t) \in V^j \Leftrightarrow f\left(\frac{t}{2}\right) \in V^{j+1} \tag{10c}$$

$$\lim_{j \to +\infty} V^j = \bigcap_{j=-\infty}^{\infty} V^j = \{0\} \tag{10d}$$

$$\lim_{j \to -\infty} V^j = \mathrm{closure}\left(\bigcup_{j=-\infty}^{\infty} V^j \right) = L^2(R) \tag{10e}$$

A Riesz basis of V^0 exists. (10f)

An orthogonal basis of V^j for all $j \in Z$ can be always constructed and is denoted by a family $\{\phi_n^j(x), n \in Z\}$ of the single function ϕ. This function ϕ, called a scaling function, is dilated and translated to generate $\phi_n^j(x)$:

$$\phi_n^j(x) = \frac{1}{\sqrt{2^j}} \phi\left(\frac{x - 2^j n}{2^j} \right) \tag{11}$$

Though a non-orthogonal Riesz basis can be used, we will work mainly with orthogonal bases in order to clarify the present development.

The scaling function generating an orthogonal basis is orthogonal with respect to its integer translation. This can be stated as:

$$\langle \phi(x), \phi(x-n) \rangle \equiv \int_{-\infty}^{\infty} \phi(x)\phi^*(x-n)\,\mathrm{d}t = \delta_n \tag{12}$$

In Eq. (12), the superscript $*$ denotes a complex conjugate. The discrete Dirac delta δ_n is defined as:

$$\delta_n = \begin{cases} 1 & \text{if } n = 0 \\ 0 & \text{else} \end{cases} \tag{13}$$

The notation $\langle\ \rangle$, representing an inner product, will be used in the subsequent development. The causality condition (10b) allows a two-scale relationship such that

$$\frac{1}{\sqrt{2}}\phi\left(\frac{x}{2}\right) = \sum_{n=-\infty}^{\infty} h_n \phi(x-n) \tag{14}$$

where h_n can be written as:

$$h_n = \langle \frac{1}{\sqrt{2}}\phi\left(\frac{x}{2}\right), \phi(x-n) \rangle \tag{15}$$

The coefficient h_n is usually viewed as a low pass filter in signal processing.

It is useful to introduce the orthogonal projection of f over V^j such that

$$P_{V^j} f = \sum_{n=-\infty}^{\infty} a_n^j \phi_n^j(x) \tag{16}$$

where a_n^j denotes the coefficient at the scale 2^j:

$$a_n^j = \langle f, \phi_n^j \rangle \tag{17}$$

When the resolution 2^{-j} goes to zero, all the detail of f is lost due to property (10d). This may be expressed as:

$$\lim_{j \to +\infty} \| P_{V^j} f \| = 0 \tag{18}$$

where the L^2-norm $\|f\|$ of a function f is defined as:

$$\|f\| = \left[\int_{-\infty}^{\infty} |f|^2\,\mathrm{d}x \right]^{\frac{1}{2}} \tag{19}$$

On the other hand, when the resolution 2^{-j} goes to $+\infty$, the original function f can be completely recovered:

$$\lim_{j \to -\infty} \| f - P_{V^j} f \| = 0 \tag{20}$$

Since V^j is included in V^{j-1}, it is possible to construct the orthogonal complement W^j as:

$$V^{j-1} = V^j \oplus W^j \tag{21}$$

where $\oplus$ represents the direct sum. Subsequently, the orthogonal projection of f on V^{j-1} can be decomposed as the sum of the orthogonal projection on V^j and W^j:

$$P_{V^{j-1}} f = P_{V^j} f + P_{W^j} f \tag{22}$$

Note that it is possible to construct an orthogonal basis $\{\psi_n^j\}_{(n,\, j\in Z)}$ of W^j by scaling and translating a single function called a wavelet ψ:

$$\psi_n^j(x) = \frac{1}{\sqrt{2^j}} \psi\left(\frac{x - 2^j n}{2^j}\right) \tag{23}$$

Furthermore, the wavelet $\psi(x)$ can be constructed from the scaling function $\phi(x)$ as:

$$\psi(x) = \sqrt{2} \sum_{n=-\infty}^{\infty} g_n \phi(2x - n) \tag{24}$$

The coefficient g_n, which is often referred to as the conjugate mirror filter of h_n, can be obtained from h_n:

$$g_n = (-1)^{1-n} h_{1-n} \tag{25}$$

The wavelet also has orthogonality with respect to integer translation:

$$\langle \psi(x), \psi(x - n) \rangle = \delta_n \tag{26}$$

Utilizing Eqs. (10e) and (20), the L^2 space may be decomposed as

$$L^2(R) = \oplus_{j=-\infty}^{\infty} W^j \tag{27}$$

Likewise, the decomposition in the following form is possible as long as $L < J$:

$$V^L = \oplus_{k=L+1}^{J} W^k \oplus V^J \tag{28}$$

Property (28) plays an important role in dealing with a discrete sequence of data.

As in Eq. (16), the orthogonal projection of f on W^j can be written as

$$P_{W^j} f = \sum_{n=-\infty}^{\infty} d_n^j \psi_n^j(x) \tag{29}$$

where

$$d_n^j = \langle f, \psi_n^j \rangle \tag{30}$$

It is important to realize that the coefficient d_n^j can be also viewed as the discrete value evaluated at $(s = 2^j, u = 2^j n)$ in the following continuous wavelet transform $WT_f(u, s)$:

$$WT_f(u, s) = \int_{-\infty}^{\infty} f(x) \frac{1}{\sqrt{s}} \psi^*\left(\frac{x - u}{s}\right) \mathrm{d}x \tag{31}$$

In order to reconstruct f from $WT_f(u, s)$, the wavelet ψ must satisfy at least the following condition (the exact reconstruction condition is called the admissibility condition; see Mallat (1998)):

$$\int_{-\infty}^{\infty} \psi(x)\,\mathrm{d}x = 0 \tag{32}$$

Daubechies (1988) showed that it is possible to construct orthogonal wavelet $\psi(x)$ with a finite support having p vanishing moments. If a wavelet $\psi(x)$ has p vanishing moments, the wavelet satisfies the following condition:

$$\int_{-\infty}^{\infty} x^k \psi(x)\,\mathrm{d}x = 0 \quad \text{for } 0 \le k < p \tag{33}$$

Because wavelets have properties (32) and (33), the wavelet transform WT_f captures sudden variations of a function f very effectively. When a function f varies rapidly or has some singularity within the support of a wavelet, WT_f gives large values. The discrete version d_n^j of WT_f has the same property. Mallat (1989) has developed Mallat's algorithm for fast computation of d_n^{j+1} and a_n^{j+1} from a_n^j.

Daubechies (1988) has constructed a family of the Daubechies orthogonal real wavelets having the minimum support size $2p-1$ while the wavelets have p vanishing moments. When $p=1$, the Daubechies wavelet reduces to the Haar wavelet (Haar, 1910) such that:

$$\psi(x) = \begin{cases} -1 & \text{if } 0 \le x < \dfrac{1}{2} \\ 1 & \text{if } \dfrac{1}{2} \le x < 1 \\ 0 & \text{otherwise} \end{cases} \tag{34}$$

the corresponding Haar scaling function $\phi(x)$ is:

$$\phi(x) = \begin{cases} 1 & \text{if } 0 \le x < 1 \\ 0 & \text{otherwise} \end{cases} \tag{35}$$

Meyer (1992) and Mallat (1989) showed that the scaling function and the wavelet can be constructed once the corresponding filter coefficient h_n in Eq. (14) is known. The filter coefficients h_n and g_n corresponding to the Haar scaling and wavelet are simply

$$h_n = \begin{cases} \dfrac{1}{\sqrt{2}} & \text{for } n = 0, 1 \\ 0 & \text{otherwise} \end{cases} \tag{36}$$

$$g_n = \begin{cases} -\dfrac{1}{\sqrt{2}} & \text{for } n = 0 \\ \dfrac{1}{\sqrt{2}} & \text{for } n = 1 \end{cases} \tag{37}$$

The Daubechies wavelet with $p=2$ (denoted by D2) can be characterized by its filter coefficients:

$$h_0 = 0.482962913145, \qquad h_1 = 0.836516303738$$

$$h_2 = 0.224143868042, \qquad h_3 = -0.129409522551 \tag{38}$$

When a set of one-dimensional discrete data $\boldsymbol{a}^0$ is given,

$$\boldsymbol{a}^0 = \left\{a_n^0\right\}^{\mathrm{T}} \quad (0 \le n \le N_e - 1) \tag{39}$$

one may assume that a_n^0 is the coefficient of a certain function in Eq. (17) with $j = 0$. Using decomposition rule (28), this set of data can be represented by its orthogonal wavelet decomposition up to the scale 2^J:

$$\hat{\boldsymbol{a}}^J = \left\{\boldsymbol{a}^J, \boldsymbol{d}^J, \boldsymbol{d}^{J-1}, \ldots, \boldsymbol{d}^1\right\}^{\mathrm{T}} = \left\{\hat{a}_n^J\right\}^{\mathrm{T}} \quad 0 \le n \le N_e - 1 \tag{40}$$

$$\boldsymbol{d}^j = \left\{d_n^j\right\}^{\mathrm{T}} \quad 0 \le n \le 2^{-j}N_e - 1, \quad 1 \le j \le J \tag{41a}$$

$$\boldsymbol{a}^J = \left\{a_n^j\right\}^{\mathrm{T}} \quad 0 \le n \le 2^{-j}N_e - 1 \tag{41b}$$

In Eq. (41), $\boldsymbol{d}^j$ are the wavelet coefficients at scale 2^j and $\boldsymbol{a}^J$ is the remaining approximation at a coarse scale of 2^J. The computation of the coefficients d_n^j and a_n^J can be carried out efficiently by the fast filter bank algorithm (Mallat, 1989) depicted in Fig. 1.

Fig. 1 shows that a fast forward wavelet transformation can be computed with cascade filtering of $\bar{h}_n$ and $\bar{g}_n$ followed by a subsampling factor of 2 where $\bar{h}_n$ and $\bar{g}_n$ are given by

$$\bar{h}_n = h_{-n}, \qquad \bar{g}_n = g_{-n} \tag{42}$$

The explicit expression of the fast filter bank algorithm depicted in Fig. 1 is as follows: At the decomposition

$$a_m^{j+1} = \sum_{n=-\infty}^{\infty} h_{n-2m} a_n^j \tag{43a}$$

$$d_m^{j+1} = \sum_{n=-\infty}^{\infty} g_{n-2m} a_n^j \tag{43b}$$

At the reconstruction

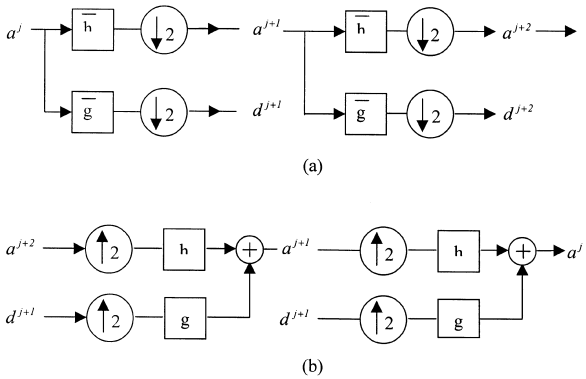

Fig. 1. Fast filter bank algorithm ($\bar{h}_n = h_{-n}, \bar{g}_n = g_{-n}$) for (a) a forward wavelet transform and (b) an inverse wavelet transform.

$$a_m^j = \sum_{n=-\infty}^{\infty} h_{m-2n} a_n^{j+1} + \sum_{n=-\infty}^{\infty} g_{m-2n} d_n^{j+1} \tag{44}$$

A finite discrete signal is usually made periodic so that the calculation of $\boldsymbol{d}^j (j = 1, 2, \ldots, J)$ and $\boldsymbol{a}^J$ are usually performed by a circular convolution (see Mallat, 1998). However, only the Haar wavelet has no border (or boundary) effect under periodization.

Although the wavelet decomposition and reconstruction are conducted using the filter bank algorithm, it may be convenient to view the decomposition and reconstruction in Eqs. (43) and (44) as linear transformations $\boldsymbol{T}$ and $\boldsymbol{IT}$ such that

$$\hat{\boldsymbol{a}}^J = \boldsymbol{T} \cdot \boldsymbol{a}^0 \tag{45}$$

$$\boldsymbol{a}^0 = \boldsymbol{IT} \cdot \hat{\boldsymbol{a}}^J = \boldsymbol{T}^{-1} \cdot \hat{\boldsymbol{a}}^J \tag{46}$$

where $\boldsymbol{T}$ and $\boldsymbol{IT}$ are $N_e \times N_e$ nonsingular square matrices.

For orthogonal wavelet transforms, one can show that:

$$\boldsymbol{T}^{-1} = \boldsymbol{T}^{\mathrm{T}} \tag{47}$$

In a two-dimensional case, we consider separable multi-resolutions based on the tensor product space as:

$$V_2^j = V^j \otimes V^j \tag{48}$$

and the space V_2^{j-1} can be decomposed as:

$$V_2^{j-1} = V_2^j \otimes W_2^j \tag{49}$$

where

$$W_2^j = \left(V^j \otimes W^j\right) \oplus \left(W^j \otimes V^j\right) \oplus \left(W^j \otimes W^j\right) \tag{50}$$

The scaling function and the wavelet in $L^2(R^2)$ can be constructed from the tensor product of a one-dimensional scaling function ϕ and a wavelet ψ as:

Scaling function:

$$\phi(x, y) = \phi(x)\phi(y) \tag{51}$$

Wavelets:

$${}^1\psi(x, y) = \phi(x)\psi(y) \tag{52a}$$

$${}^2\psi(x, y) = \psi(x)\phi(y) \tag{52b}$$

$${}^3\psi(x, y) = \psi(x)\psi(y) \tag{52c}$$

The families $\{\phi_{n,m}^j\}_{(n,\, m \in Z)}$ construct an orthonormal basis of V_2^j and the families $\{{}^1\psi_{n,m}^j(x, y), {}^2\psi_{n,m}^j(x, y), {}^3\psi_{n,m}^j(x, y)\}_{(j,\, n,\, m) \in Z}$ form an orthonormal basis of W_2^j. The definition of $\phi_{n,m}^j$ and ${}^k\psi_{n,m}^j$ is:

$$\phi^{j}_{n,m}(x,y) = \frac{1}{2^{j}}\phi\left(\frac{x-2^{j}n}{2^{j}}, \frac{y-2^{j}m}{2^{j}}\right) \tag{53a}$$

$${}^{k}\psi^{j}_{n,m}(x,y) = \frac{1}{2^{j}}{}^{k}\psi\left(\frac{x-2^{j}n}{2^{j}}, \frac{y-2^{j}m}{2^{j}}\right) \quad (k=1,2,3) \tag{53b}$$

As in the one-dimensional case, the projection onto V_2^j and W_2^j can be written as:

$$P_{V_2^j} f = \sum_{n=-\infty}^{\infty}\sum_{m=-\infty}^{\infty} a^{j}_{n,m}\phi^{j}_{n,m}(x,y) \tag{54}$$

$$P_{W_2^j} f = \sum_{n=-\infty}^{\infty}\sum_{m=-\infty}^{\infty}\sum_{k=1}^{3} {}^{k}d^{j}_{n,m}\,{}^{k}\psi^{j}_{n,m}(x,y) \tag{55}$$

where the coefficients $a^{j}_{n,m}$ and ${}^{k}d^{j}_{n,m}$ are found as:

$$a^{j}_{n,m} = \langle f, \phi^{j}_{n,m}\rangle = \int_{-\infty}^{\infty}\int_{-\infty}^{\infty} f(x,y)\phi^{j}_{n,m}(x,y)\,\mathrm{d}x\,\mathrm{d}y \tag{56}$$

$${}^{k}d^{j}_{n,m} = \langle f, {}^{k}\psi^{j}_{n,m}\rangle = \int_{-\infty}^{\infty}\int_{-\infty}^{\infty} f(x,y)\,{}^{k}\psi^{j}_{n,m}(x,y)\,\mathrm{d}x\,\mathrm{d}y \tag{57}$$

The fast algorithm for the decomposition of $a^{j}_{n,m}$ into $a^{j+1}_{n,m}$ and ${}^{k}d^{j+1}_{n,m}$, and the reconstruction of $a^{j}_{n,m}$ from $a^{j+1}_{n,m}$ and ${}^{k}d^{j+1}_{n,m}$ is basically the same as the one-dimensional filter bank. When a set of two-dimensional discrete data $a^{0}_{n,m}$ is given as

$$\boldsymbol{a}^{0} = \left[a^{0}_{n,m}\right](0\le n\le N_e-1,\ 0\le m\le M_e-1) \tag{58}$$

its orthogonal wavelet representation up to a coarse scale J may be split into $3J+1$ blocks as shown in Fig. 2.

It is convenient to introduce the following notation in the case of the two-dimensional data:

$$\boldsymbol{a}^{J} = \left[a^{J}_{n,m}\right]\left(0\le n\le 2^{-J}N_e-1,\ 0\le m\le 2^{-J}M_e-1\right) \tag{59}$$

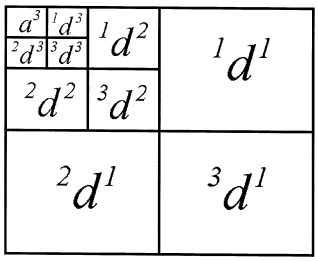

Fig. 2. Separable wavelet transform of a two-dimensional image up to level $J=3$.

$$ {}^{k}\boldsymbol{d}^{j} = \left[{}^{k}d^{j}_{n,m} \right] \left(0 \le n \le 2^{-j}N_e - 1,\ 0 \le m \le 2^{-j}M_e - 1,\ k = 1, 2, 3 \right) \tag{60} $$

We also define $\hat{\boldsymbol{a}}^J$ as:

$$ \hat{\boldsymbol{a}}^J = \left[\boldsymbol{a}^J, \left\{ {}^{1}\boldsymbol{d}^J, {}^{2}\boldsymbol{d}^J, {}^{3}\boldsymbol{d}^J \right\}, \left\{ {}^{1}\boldsymbol{d}^{J-1}, {}^{2}\boldsymbol{d}^{J-1}, {}^{3}\boldsymbol{d}^{J-1} \right\}, \ldots, \left\{ {}^{1}\boldsymbol{d}^{1}, {}^{2}\boldsymbol{d}^{1}, {}^{3}\boldsymbol{d}^{1} \right\} \right] = \left[\hat{a}^J_{n,m} \right]^{\mathrm{T}} $$
$$ (0 \le n \le N_e - 1,\ 0 \le m \le M_e - 1) \tag{61} $$

The location of $\boldsymbol{a}^J$ and ${}^{k}\boldsymbol{d}^{j}$ in the two-dimensional array $\hat{\boldsymbol{a}}^J$ for $J = 3$ is depicted in Fig. 2.

It is worth mentioning that the coefficients of large amplitude in ${}^{1}\boldsymbol{d}^{j}$, ${}^{2}\boldsymbol{d}^{j}$ and ${}^{3}\boldsymbol{d}^{j}$ correspond respectively to horizontal edges, vertical edges, and corners of a two-dimensional image. Since ${}^{1}\boldsymbol{d}^{j}$, ${}^{2}\boldsymbol{d}^{j}$ and ${}^{3}\boldsymbol{d}^{j}$ correspond to edges and corners, we anticipate that optimization in the wavelet space will be very efficient; the boundary of an optimized structure can be effectively captured due to wavelet properties expressed by Eqs. (32) and (33).

As in the one-dimensional case, one can interpret the wavelet transform of $\boldsymbol{a}^J$ into $\hat{\boldsymbol{a}}^J$ as a linear transformation:

$$ \hat{\boldsymbol{a}}^J = \left(\boldsymbol{T}_x \otimes \boldsymbol{T}_y \right) \boldsymbol{a}^0 \tag{62} $$

and

$$ \boldsymbol{a}^0 = \left(\boldsymbol{T}_x \otimes \boldsymbol{T}_y \right)^{-1} \hat{\boldsymbol{a}}^J \tag{63a} $$

$$ \boldsymbol{a}^0 = \left(\boldsymbol{T}_x \otimes \boldsymbol{T}_y \right)^{T} \hat{\boldsymbol{a}}^J \quad \text{for orthogonal transforms.} \tag{63b} $$

4. Topology optimization in a wavelet space

4.1. Wavelet transform of direct density variables

As pointed out earlier, the design space will be transformed from the discrete density space to a new space by the wavelet transform for multi-resolution multi-scale topology optimization. However, the side constraint (7) becomes complicated in the wavelet-transformed variable space (which will be called the wavelet space) so that the wavelet-space design optimization is not quite practical. To illustrate the complication in the wavelet space, consider a one-dimensional case with only two design variables (ρ_1, ρ_2). Among various wavelet transforms, the simplest Haar wavelet transform is selected without the loss of generality.

Using Eqs. (36), (37) and (43), one can find the relation between the direct density variables (ρ_1, ρ_2) and the wavelet transformed variables $(\hat{\rho}_1, \hat{\rho}_2)$ as:

$$ \hat{\rho}_1 = \frac{1}{\sqrt{2}}(\rho_1 - \rho_2) $$

$$ \hat{\rho}_2 = \frac{1}{\sqrt{2}}(\rho_1 + \rho_2) \tag{64} $$

Observe that in the space of $\hat{\rho}_1$ and $\hat{\rho}_2$, the side constraint (7) (with $\varepsilon = 0$) becomes,

$$\hat{\rho}_2 \le \hat{\rho}_1 \tag{65a}$$

$$\hat{\rho}_2 \ge \hat{\rho}_1 - \sqrt{2} \tag{65b}$$

$$\hat{\rho}_2 \ge -\hat{\rho}_1 \tag{65c}$$

$$\hat{\rho}_2 \le -\hat{\rho}_1 + \sqrt{2} \tag{65d}$$

The constraints in the $\boldsymbol{\rho}$ and $\hat{\boldsymbol{\rho}}$ spaces are depicted in Fig. 3. As clearly seen in Fig. 3, the side constraints in the wavelet-transformed space are not so simple as Eq. (7), and substantial numerical complexity arises. Since wavelet transforms using other wavelets than the Haar wavelet involve more than two density variables, the constraint equations in terms of wavelet transformed variables involve more than two variables. In two-dimensional situations, even the determination of the constraints in the transformed variables is cumbersome. Therefore, it appears that optimization in this wavelet-

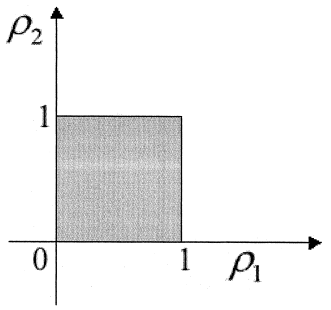

(a)

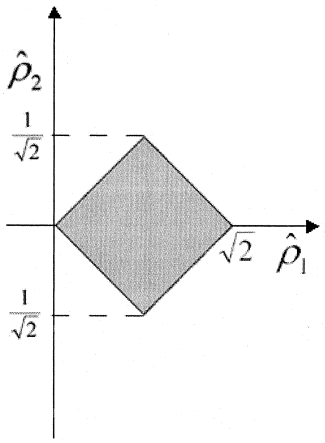

(b)

Fig. 3. Side constraint in terms of (a) (ρ_1, ρ_2) and (b) $(\hat{\rho}_1, \hat{\rho}_2)$.

transformed space is not very practical or useful although wavelets may catch image or optimized structure boundaries effectively.

4.2. The introduction of intermediate variables

Since we will consider two-dimensional problems, it is convenient to treat $\boldsymbol{\rho}$ in Eq. (3) now as a two-dimensional array such that

$$\boldsymbol{\rho} = [\rho_{nm}](0 \le n \le N_e - 1,\ 0 \le m \le M_e - 1) \tag{66}$$

where

$$\rho_{nm} = \rho_e \quad \text{with } e = e(n, m) \tag{67}$$

To overcome the difficulty discussed in Section 4.1, we propose to introduce intermediate variables a^0_{nm} such that:

$$\rho_{nm} = g\left(a^0_{nm}\right)(0 \le n \le N_e - 1,\ 0 \le m \le M_e - 1) \tag{68}$$

where the transformation g is selected to satisfy the following criteria:

1. One-to-one correspondence between ρ_{nm} and a^0_{nm} must be ensured.
2. Under the transformation g, the side constraint expressed by Eq. (7) should be relaxed or removed in the space of a^0_{nm}.

One can show that the following transformations satisfy the criteria above:

$$\rho_{nm} = \frac{1}{\pi} a \tan\left(S a^0_{nm}\right) + \frac{1}{2}, \quad \text{where } S \in R^+ \tag{69}$$

$$\rho_{nm} = \frac{1 - \exp\left(-S a^0_{nm}\right)}{2 + 2\exp\left(-S a^0_{nm}\right)} + \frac{1}{2}, \quad \text{where } S \in R^+ \tag{70}$$

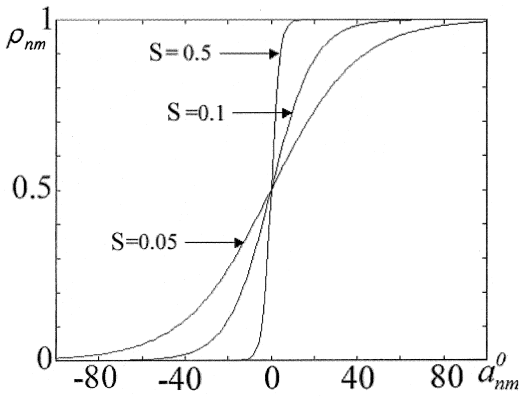

Fig. 4. The Sigmoid function with various of S.

$$\rho_{nm} = \frac{1}{1+\exp\left(-Sa^0_{nm}\right)}, \quad \text{where } S \in R^+ \tag{71}$$

It is remarkable that the side constraint (7) is actually eliminated by any of the transformations in Eqs. (69)–(71):

$$-\infty < a^0_{nm} < \infty \tag{72}$$

Among the three transformation functions given in Eqs. (69)–(71), the transformation in Eq. (71) is selected for the present analysis though other transforms may be selected.

The function appearing in Eq. (71) is usually referred to as the Sigmoid function and plotted in Fig. 4. The Sigmoid function is one of S-shaped 'squashing functions'. This function maps a real value that may be arbitrarily large in magnitude (positive or negative) to a real value that lies within some narrow range. The value of the parameter S changes the shape of the Sigmoid function and may affect the convergence rate in the optimization process. The effects of the values of S on the solution convergence will be examined along with numerical examples.

Now the wavelet transform will be applied to the two dimensional discrete data a^0_{nm} which are mapped from ρ_{nm}. Once the resolution level J in Eq. (62) is selected, $\hat{\boldsymbol{a}}^J$ can be easily obtained by Mallat's algorithm (Mallat, 1989).

4.3. Sensitivity analysis

To find an optimal solution in the $\hat{\boldsymbol{a}}^J$ space, the sensitivities of the mean compliance L and constraints with respect to $\hat{\boldsymbol{a}}^J$ are required. It is straightforward to obtain:

$$\frac{\partial L}{\partial \hat{a}^J_{nm}} = \sum_{i=0}^{N_e-1}\sum_{j=0}^{M_e-1} \frac{\partial L}{\partial a^0_{ij}} \frac{\partial a^0_{ij}}{\partial \hat{a}^J_{nm}} \tag{73}$$

Eq. (73) can be written in compact form as:

$$\frac{\partial L}{\partial \hat{\mathrm{a}}^J} = \left(\boldsymbol{T}_x \otimes \boldsymbol{T}_y\right) \frac{\partial L}{\partial \boldsymbol{a}^0} \tag{74}$$

where

$$\frac{\partial L}{\partial \boldsymbol{a}^0} = \left[\frac{\partial L}{\partial a^0_{nm}}\right], \ \frac{\partial L}{\partial \hat{\boldsymbol{a}}^J} = \left[\frac{\partial L}{\partial \hat{a}^J_{nm}}\right] \quad 0 \le n \le N_e - 1,\ 0 \le m \le M_e - 1 \tag{75}$$

The sensitivity of L with respect to $\boldsymbol{a}^0_{ij}$ is simple to compute:

$$\frac{\partial L}{\partial a^0_{nm}} = \frac{\partial L}{\partial \rho_{nm}} \frac{\partial \rho_{nm}}{\partial a^0_{nm}} \tag{76}$$

where $\partial \rho_{nm}/\partial a^0_{nm}$ is found from Eq. (71).

Similarly, the sensitivity of the constraint (2) with respect to $\hat{\boldsymbol{a}}^J$ is

$$\frac{\partial H}{\partial \hat{\boldsymbol{a}}^J} = \left(\boldsymbol{T}_x \otimes \boldsymbol{T}_y\right) \frac{\partial H}{\partial \boldsymbol{a}^0} \tag{77}$$

where

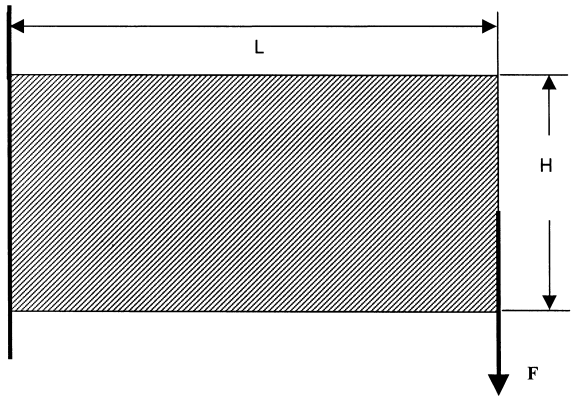

Fig. 5. The Michell benchmark problem (L = 16, H = 10, Poisson's ratio = 0.3).

$$\frac{\partial H}{\partial a^0_{nm}} = \frac{\partial H}{\partial \rho_{nm}} \frac{\partial \rho_{nm}}{\partial a^0_{nm}} \tag{78}$$

Note again that there is no side constraint imposed on the design variable $\hat{\boldsymbol{a}}^J$.

5. Multi-resolution multi-scale topology optimization

The formulation for topology optimization in the wavelet space was given in the previous section. In this section, we will discuss the implementation of multi-resolution topology optimization in the wavelet space. The Michell benchmark, shown in Fig. 5, will be used as the first test problem. The objective of this problem is to find a structure with minimal compliance subjected to the mass constraint of 37.5%. The geometry and material data are given in the figure. Two finite element models with Mesh 1 and Mesh 2, shown in Fig. 6, will be used for design optimization. The total numbers of elements for Mesh 1 and Mesh 2 are $2^N \times 2^M = 512$ ($N = 5$, $M = 4$) and $2^N \times 2^M = 2048$ ($N = 6$, $M = 5$), respectively.

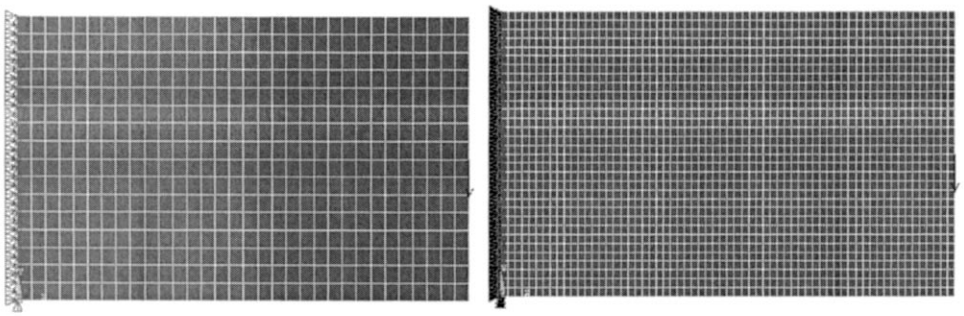

Fig. 6. Finite element discretization for the Michell benchmark problem for (a) Mesh 1 (512 elements) and (b) Mesh 2 (2048 elements).

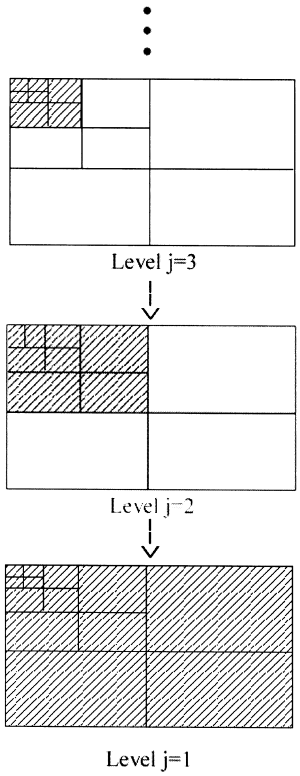

Fig. 7. Description of the multi-level design process.

For all the numerical work, we use 8 node plane stress elements. Though checkerboards can be suppressed by the wavelets (Kim and Kim, 1999; Poulsen, 1999), we use higher order elements to focus on more fundamental numerical instabilities.

The motivation for multi-resolution multi-scale topology optimization is that design should progress from a low to a high resolution level. However, existing design optimization schemes have no notion of resolution and thus yield optimized results directly at one resolution level. To understand this, consider an artist's drawing process. The initial drawing sketches the boundary of an object (say, a man's face) with a thick brush (a long scale) and more details are added wth thinner brushes (shorter scales) on the sketch as the drawing progresses. This drawing process is basically the same as the multi-resolution

Table 1
Definition of Resolution Level (the case with Mesh 2 having $2^M \times 2^N = 2^6 \times 2^5$ elements is considered)

Definition	Active design variables	Number of design variables	Remark
Resolution Level 1	$\boldsymbol{a}^6$, ${}^2\boldsymbol{d}^6$, $\{{}^k\boldsymbol{d}^5\},\ldots,\{{}^k d^1\}$ for $k = 1, 2, 3$	$2^6 \times 2^5$	Full level
Resolution Level j	$\boldsymbol{a}^J$, ${}^k\boldsymbol{d}^J$, ${}^k\boldsymbol{d}^{J-1},\ldots,{}^k\boldsymbol{d}^j$ $k = 1, 2, 3$	$2^{6-j+1} \times 2^{5-j+1}$	Intermediate level
Resolution Level 6	$\boldsymbol{a}^6$, ${}^2\boldsymbol{d}^6$	2	Non-trivial lowest starting level for MTOP
Resolution Level 7	$\boldsymbol{a}^6$	1	Trivial case

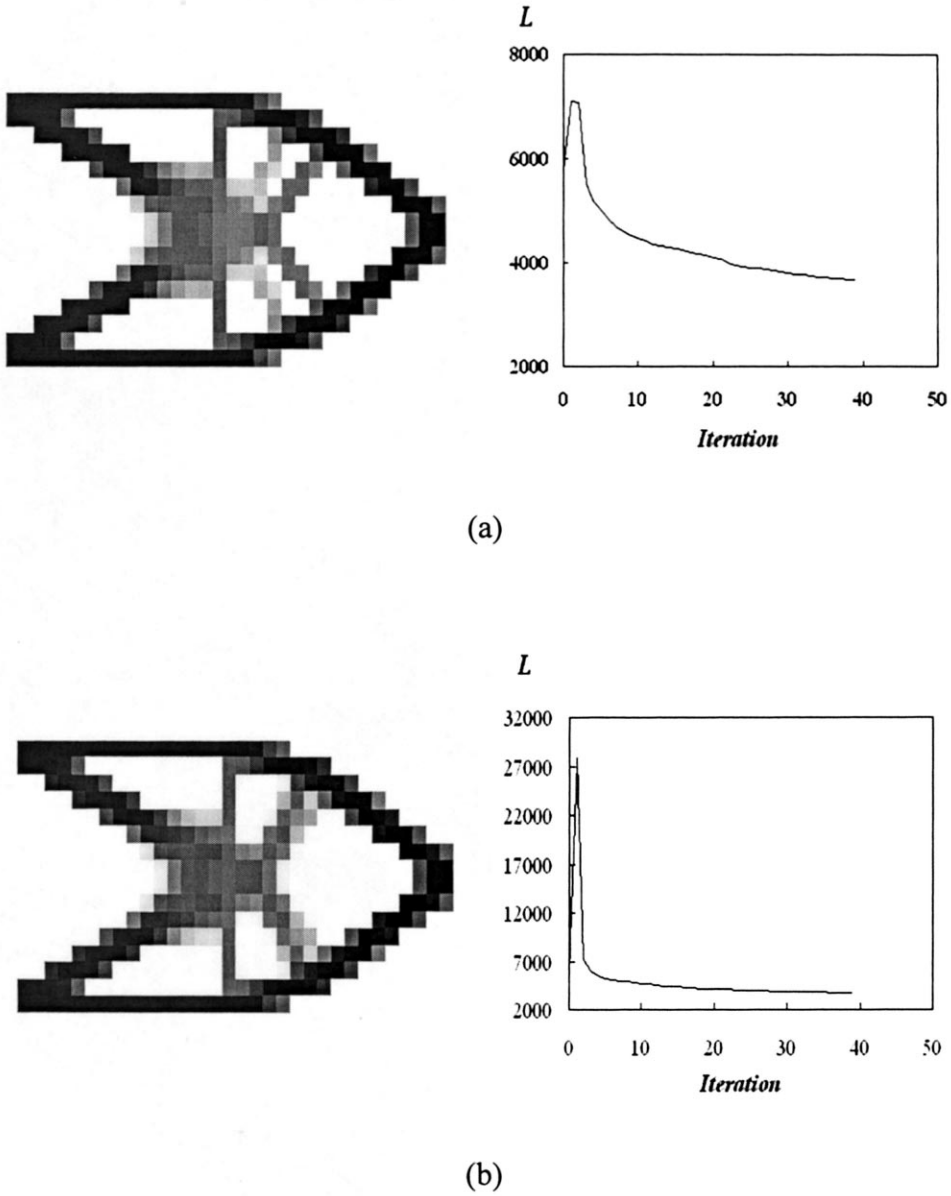

Fig. 8. Optimized results obtained by the modified feasible direction method for Mesh 1, (a) in the direct density space and (b) in the wavelet space at full resolution (no post-processing).

multi-scale topology optimization that we will carry out. We postulate that this progressive drawing concept applies equally to structural topology optimization.

Referring to Fig. 2, the multi-resolution design process may be viewed as the process depicted in Fig. 7. The shadowed region in Fig. 7 is proportional to the number of the design variables used at each level. More design variables including shorter scales are used as higher resolution is pursued. As

explained earlier, the present multi-resolution multi-scale analysis may be realized most effectively in the wavelet-transformed space $\hat{\boldsymbol{a}}^J$. Note that at low resolution, only the design variables with long scales are used. However, at high resolution, both long- and short-scaled design variables are used.

In the multi-resolution multi-scale topology optimization scheme, an optimized topology at a scale of 2^j or level j will be used as an initial topology for the optimization at the next resolution, i.e., at a scale of 2^{j-1}. Before going further, it is convenient to define 'Resolution Level j' (or simply 'Level j') to refer to the level of resolution. Table 1 explains how many design variables are included in Resolution Level j

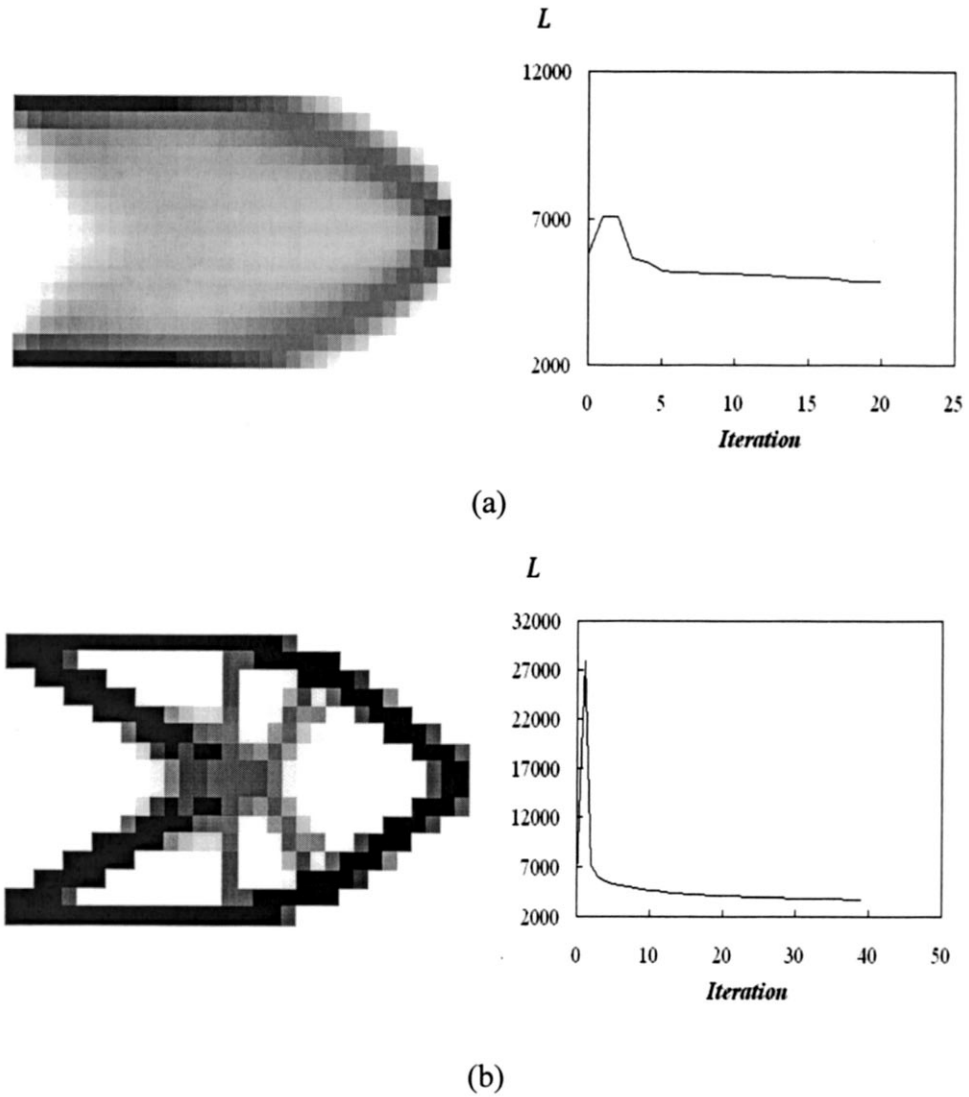

Fig. 9. Optimized results obtained by the feasible direction method for Mesh 1, (a) in the direct density space and (b) in the wavelet space at full resolution (no post-processing).

Table 2
The numbers of iterations (N_{iter}) and function (N_f) evaluations with the optimized function values (L_{opt}) for the results shown in Figs. 8 and 9

Optimizer	Density space		Wavelet space	
	N_{iter}, N_f	L_{opt}	N_{iter}, N_f	L_{opt}
FDM	31, 72	4877.56	40, 120	3740.29
MFDM	40, 530	3675.72	40, 289	3746.00

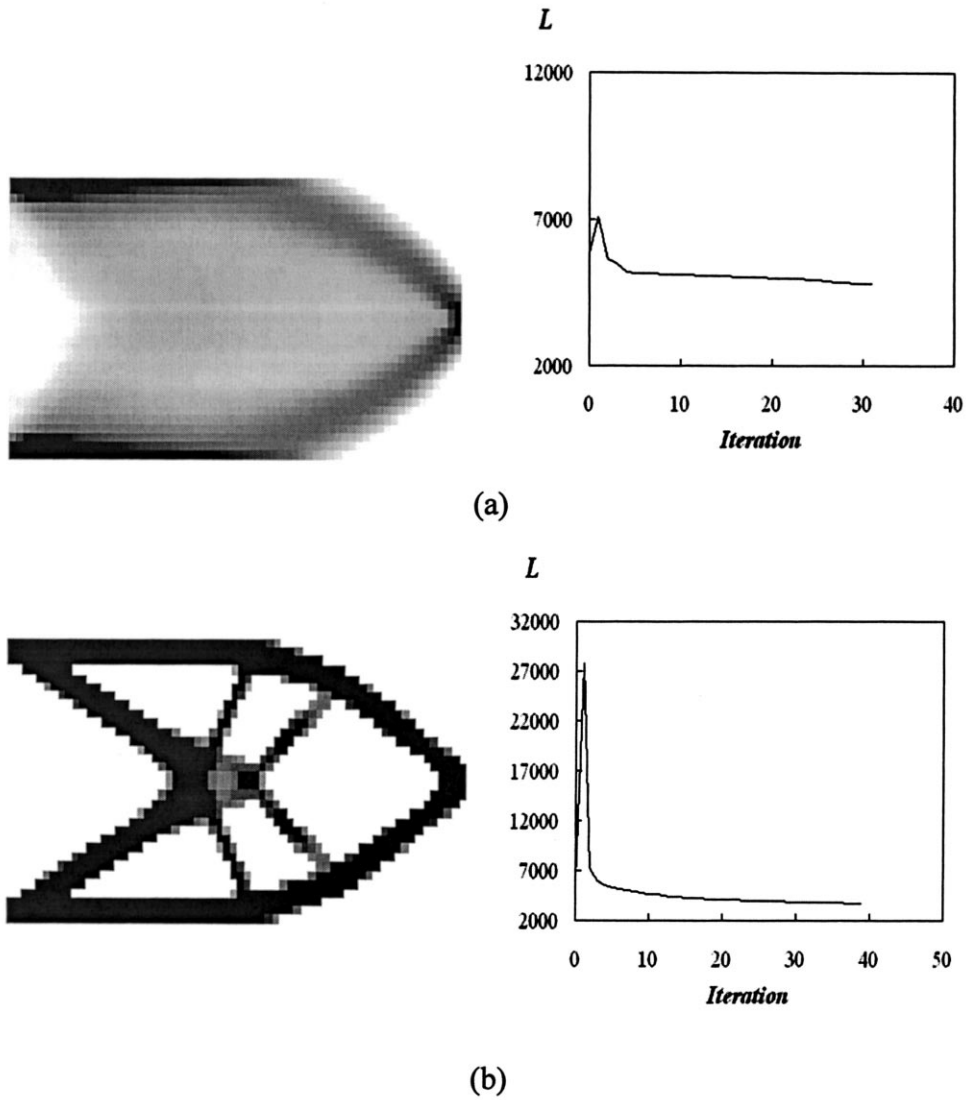

Fig. 10. Optimized results obtained by the feasible direction method for Mesh 2, (a) in the direct density space and (b) in the wavelet space at full resolution (no post-processing).

in the case of Mesh 2. Note that Resolution Level 1 corresponds to the full resolution where the number of the wavelet-based design variables is the same as the number of the original density variables.

For easy numerical implementation, the numbers N_e and M_e of the original finite elements are taken as the powers of 2 such that $N_e = 2^N$ and $M_e = 2^M$. Without the loss of generality, we assume that $N \geq M$. The lowest resolution is Resolution Level $N+1$ in which only one non-vanishing term actually represents the average density. Thus the term a^{N+1} can be easily computed from the prescribed mass constraint ratio. Note that Level $M+1$ to Level $N+1$ include the design variables corresponding to one-dimensional decompositions.

5.1. Full resolution multi-scale topology optimization

Before discussing general multi-resolution multi-scale topology optimization, we consider first the full resolution multi-scale topology optimization in the wavelet space. This is a special case of the multi-resolution multi-scale topology optimization started at Resolution Level 1. This optimization will be designated as 'FTOP' in this work. We use the methods of feasible direction (FDM) and modified feasible direction (MFDM) (Vanderplaats, 1984a) as the numerical optimizers. FDM and MFDM of ADS, the program developed by Vanderplaats (1984b), are used. Unless stated otherwise, the wavelet used for the wavelet transform is the simplest Haar wavelet. In what follows, we will compare the numerical results obtained from the wavelet-based full resolution optimization and those from the direct density-based optimization.

5.1.1. Effect of optimizers

First, we examine the effect of optimizers on the solution convergence. The results obtained by the modified feasible direction method and the feasible direction method are shown in Figs. 8 and 9, respectively. The optimized results in the direct density space and the wavelet space are given in (a) and (b). The results in Figs. 8 and 9 are based on Mesh 1. The iteration numbers and the objection function values are listed in Table 2. We used the absolute (C_a) and the relative (C_r) convergence criteria as $C_a = 0.01$ and $C_r = 0.01$. From the results given by Figs. 8 and 9 and Table 2, the following conclusions may be drawn.

1. FTOP in the wavelet space is not so sensitive to optimizers. The same configurations are obtained regardless of the optimizers in consideration. Intermediate density values are suppressed in the wavelet space optimization unlike in the density space optimization.
2. The number of function evaluations is substantially reduced when design optimization is carried out in the wavelet space.
3. For the wavelet-space optimization, the object function varies substantially during the first few iterations and then decreases monotonically to the minimum value.

Why does the optimization in the wavelet space outperform the optimization in the density space? The main reason is that wavelets have the vanishing moments as stated by Eq. (33). In the case of the Haar

Table 3
The numbers of iterations (N_{iter}) and function evaluations (N_f) with the optimized function values (L_{opt}) for varying mesh size

Optimizer	$N_e \times M_e = 512$	$N_e \times M_e = 1024$	$N_e \times M_e = 2048$
FDM	$N_{\text{iter}} = 40$, $N_f = 120$, $L_{\text{opt}} = 3740.29$	$N_{\text{iter}} = 40$, $N_f = 120$, $L_{\text{opt}} = 3457.72$	$N_{\text{iter}} = 40$, $N_f = 123$, $L_{\text{opt}} = 3485.15$
MFDM	$N_{\text{iter}} = 40$, $N_f = 289$, $L_{\text{opt}} = 2746.00$	$N_{\text{iter}} = 40$, $N_f = 336$, $L_{\text{opt}} = 3479.69$	$N_{\text{iter}} = 40$, $N_f = 362$, $L_{\text{opt}} = 3411.92$

wavelet, it has one vanishing moment ($p = 1$). This implies that the Haar wavelet can detect function discontinuities effectively. Therefore, the boundary of the optimized structure can be identified well in the wavelet space, which obviously plays a critical role in topology optimization. Furthermore, wavelets are constructed by dilating a mother wavelet so that functions or quantities having multi-scales can be well represented in the wavelet space. Due to the vanishing moment and the multi-scale properties, relatively small changes in the wavelet coefficients corresponding to long scales result in big structural topology changes (see the iteration histories shown in Figs. 8 and 9). Therefore, an optimizer can find

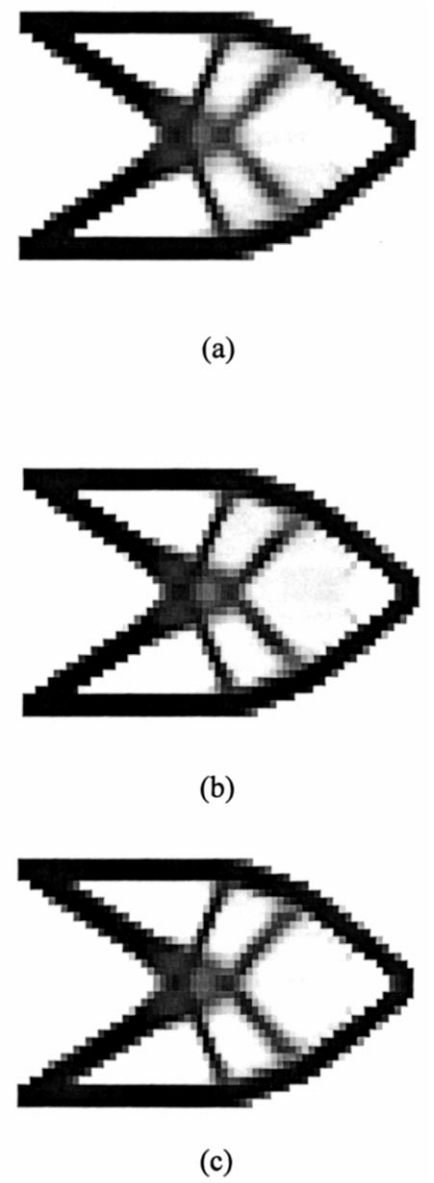

Fig. 11. FTOP results with the Sigmoid parameter equal to (a) $S = 0.01$, (b) $S = 0.3$ and (c) $S = 100$.

Table 4
The effect of the Sigmoid parameter S on the convergence

S	N_{iter}, N_f, L_{opt}
0.01	$N_{\text{iter}} = 40$, $N_f = 127$, $L_{\text{opt}} = 3511.65$
0.3	$N_{\text{iter}} = 40$, $N_f = 123$, $L_{\text{opt}} = 3485.15$
100	$N_{\text{iter}} = 40$, $N_f = 123$, $L_{\text{opt}} = 3494.34$

structure boundaries more effectively at the initial iteration stage. As shall be shown later, this idea can be realized better in the frame of multi-resolution multi-scale topology optimization.

5.1.2. Effect of mesh size

To see the effect of the mesh size on the solution convergence, we consider the same Mitchell optimization problem with Mesh 2. The results are shown in Fig. 10. As in the case of Mesh 1, the present wavelet-based full resolution multi-scale optimization gives a satisfactory result. However, both the feasible and the modified feasible direction methods for the direct density space optimization give unsatisfactory results; only the result by the feasible direction method is given in Fig. 10(a). The number of function evaluations for the converged result of Fig. 10(b) was 123. Note that unless the objective function includes an additional penalty term such as $\lambda \sum \rho_e \times (1 - \rho_e)$ in the case of the direct density space optimization, no convergence was achieved with the two mathematical programming methods in consideration.

In Table 3, we list the number of the FTOP iterations and function evaluations for the converged result with varying meshing size. The results are interesting: the total function evaluation and iteration numbers are not very sensitive to the mesh size. As explained earlier, the wavelet coefficients associated with long scales are adjusted first as these coefficients vary the structural configuration significantly. This property may be very useful in developing a more efficient optimization scheme.

Tables 2 and 3 show that smaller numbers of iterations are required by FDM when the present wavelet-based design optimization is carried out. Therefore, we will use FDM for all the numerical problems below.

5.1.3. Effect of the Sigmoid parameter S

The effect of the Sigmoid parameter S in Eq. (71) on the solution convergence also needs to be examined. Although the side constraint (7) is removed by the transform (71), the search limits of the

Fig. 12. FTOP results using the Daubechies wavelet order 2 (no post-processing).

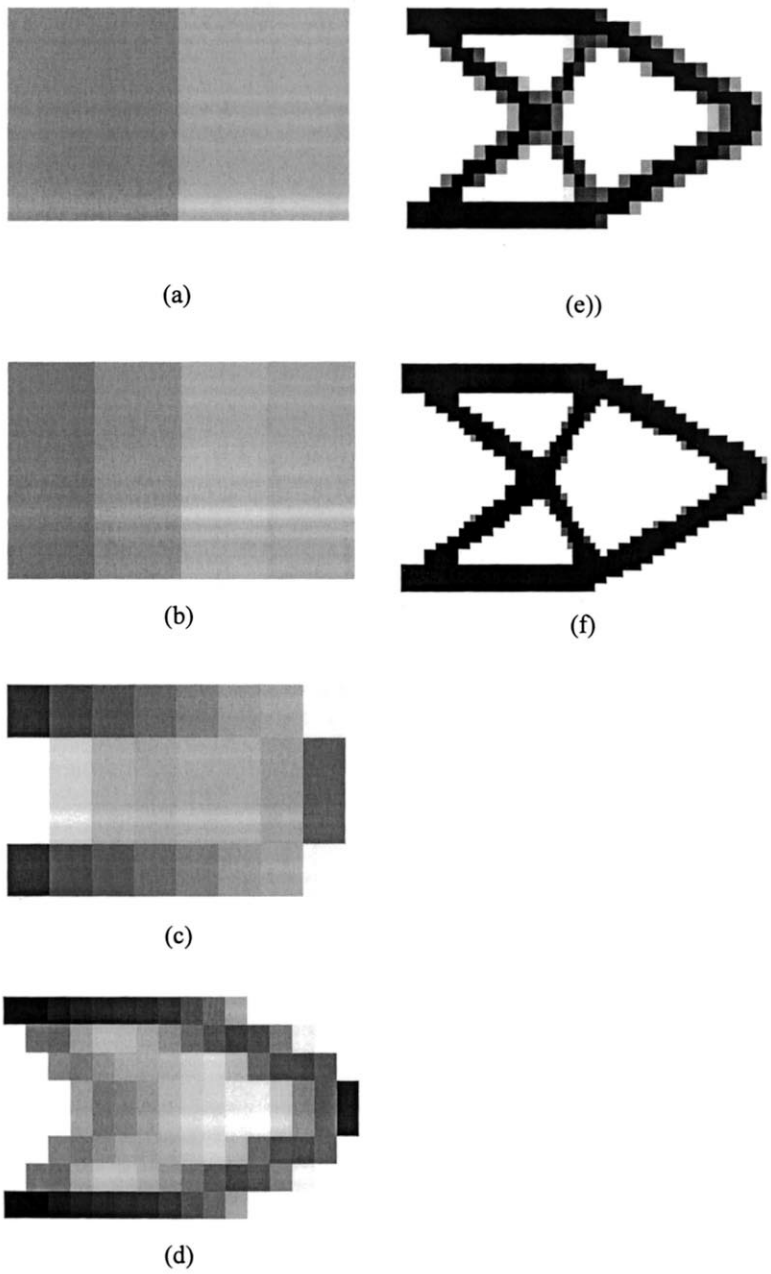

Fig. 13. Multi-resolution topology optimization started at Resolution Level 6. The results for Mesh 2 are obtained at (a) Level 6, (b) Level 5, (c) Level 4, (d) Level 3, (e) Level 2 and (f) Level 1 without post-processing.

Table 5
The results by MTOP started at Resolution Level 6

Resolution Level	N_{iter}, N_f	L_{opt}
6	5, 11	9834.322
5	4, 11	9685.278
4	24, 74	6549.451
3	24, 84	4969.323
2	39, 120	3666.04
1	10, 35	3313.36

design variables must be provided when FDM or MFDM is used. We have obtained satisfactory results for any of the following Sigmoid parameters and search limits.

$$\text{For } S = 100, \quad -1 \ll a^J_{nm}, {}^k d^{\,j}_{nm} \ll 1$$

$$\text{For } S = 0.3, \quad -100 < a^J_{nm}, {}^k d^{\,j}_{nm} < 100$$

$$\text{For } S = 0.01, \quad -1000 < a^J_{nm}, {}^k d^{\,j}_{nm} < 1000$$

Fig. 11 shows the optimized configurations for different values of S and Table 4 lists the corresponding iteration and function evaluation numbers. The feasible direction method is used for the results given in Fig. 11. The results shown in Fig. 11 and listed in Table 4 indicate that the solution convergence is virtually insensitive to the values of S, but of $S = 0.3$ is used throughout the present numerical work. However, the value of S should be so selected that the sensitivity of ρ_{nm} with respect to a^J_{nm}, ${}^k d^{\,j}_{nm}$ is not too large or small.

5.1.4. Effect of wavelets

So far, we have considered only the Haar wavelet for the wavelet transform. However, there are other wavelets having more vanishing moments. As explained earlier, the vanishing moment property of wavelets plays an important role in convergence improvement. However, wavelets with more vanishing moments have longer supports. Since the localization property of wavelets is controlled by the support size, a trade between the order of vanishing moments and the support size should be made. The Haar wavelet has the best localization property as it has the shortest support size.

Among many wavelets, we consider the orthogonal Daubechies wavelet with p vanishing moments, which is denoted by Dp. The size of the corresponding filter h is $2p$. To see the effect of the order p of vanishing moments on solutions, we take D1 ($p = 1$) and D2 ($p = 2$). Note that D1 is nothing but the Haar wavelet and the results by the Haar wavelet were already given. Fig. 12 shows the optimized results obtained with D2 for Mesh 2. Though the results by D1 (shown in Fig. 10(b)) and D2 (shown in Fig. 12) are both satisfactory, the number of intermediate density variables by D2 is smaller than that by D1. This is attributed to the fact that D2 has more vanishing moments.

Besides the orthogonal Daubechies wavelets, there are biorthogonal wavelets designed by Cohen et al. (1992). However, no attempt is made to try all available wavelets in the present work. The message is, however, is that depending on the goal of optimization, there may be optimal wavelets. More research towards this direction needs to be done.

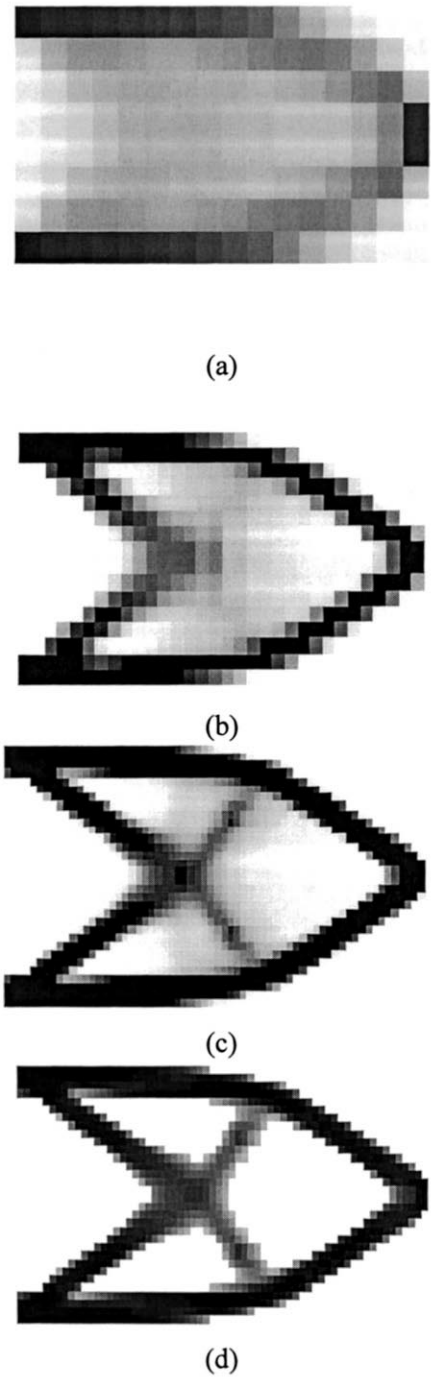

Fig. 14. Multi-resolution topology optimization started at Resolution Level 3. The results for Mesh 2 are obtained at (a) Level 3, (b) Level 2 and (c) Level 1 without post-processing. The result from (c) is post-processed to yield the result shown in (d).

Table 6
The result by MTOP started at Resolution 1 Level 3

Resolution Level	N_{iter}, N_f	L_{opt}	Convergence criteria	
			C_a[a]	C_r[b]
3	6, 18	5446.39	0.1	0.1
2	12, 37	4235.74	0.01	0.01
1	9, 49	3705.44	0.01	0.01

[a] Absolute convergence criterion.
[b] Relative convergence criterion.

5.2. Multi-resolution multi-scale topology optimization

The key idea of the multi-resolution multi-scale topology optimization (MTOP) is to start the optimization at low resolution and then to proceed to the next resolution. In this multi-resolution optimization framework, optimization may begin at any desired resolution level, say, Resolution Level j. The optimal solution obtained at Resolution Level j is then inputted as an initial guess for an optimal solution at the next resolution, i.e., Resolution Level $j-1$. This process will repeat until the final resolution reaches the highest resolution, Resolution Level 1. In this setup, the number of the wavelet-based design variables increases as the higher resolution is reached. However, the finite element mesh for the highest resolution is used for all resolution levels. We will apply MTOP based on the Haar wavelet to problems in consideration.

First we consider the MTOP started at Resolution Level 6. This resolution is the lowest nontrivial resolution level since Resolution Level 7 gives a trivial solution with $\hat{\boldsymbol{a}}^7$ corresponding to the mean density. Fig. 13 shows the results obtained at different resolution levels. Note that the result at Level j was used as the initial guess for optimization at Level $j-1$. The finite element model employed for MTOP is based on Mesh 2. Table 5 gives the number of iterations and function evaluations required for the converged results as well as the converged object function values. From the results obtained by MTOP, we have found:

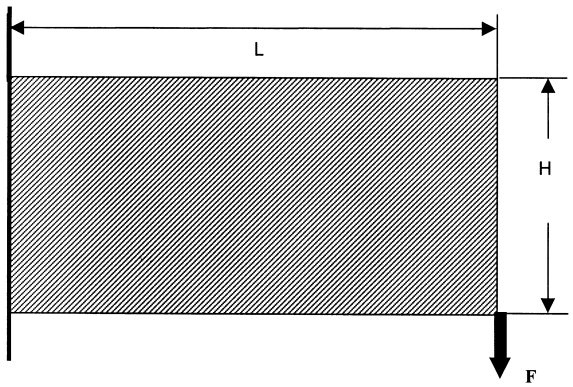

Fig. 15. A compliance minimization problem under one point load at the corner (L = 16, H = 10).

Fig. 16. The result by FTOP for the problem defined in Fig. 16 ($N_{\text{iter}} = 40$, $N_f = 124$, $L_{\text{opt}} = 3982.87$).

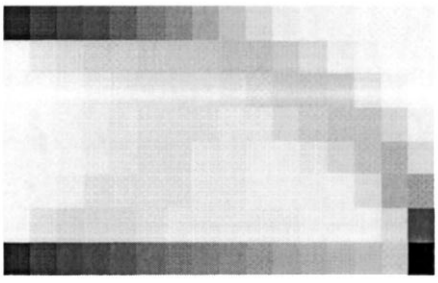

(a)

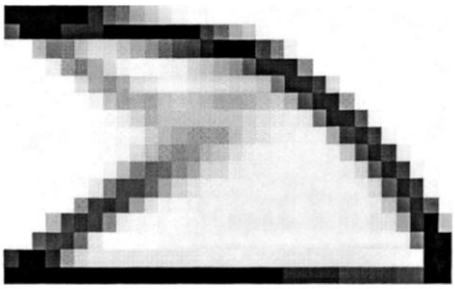

(b)

(c)

Fig. 17. MTOP started at Resolution Level 3. The results are obtained at (a) Level 3 ($N_{\text{iter}} = 6$, $N_f = 124$, $L_{\text{opt}} = 7836.92$) (b) Level 2 ($N_{\text{iter}} = 20$, $N_f = 77$, $L_{\text{opt}} = 4755.94$), and (c) Level 1 ($N_{\text{iter}} = 38$, $N_f = 137$, $L_{\text{opt}} = 3943.65$).

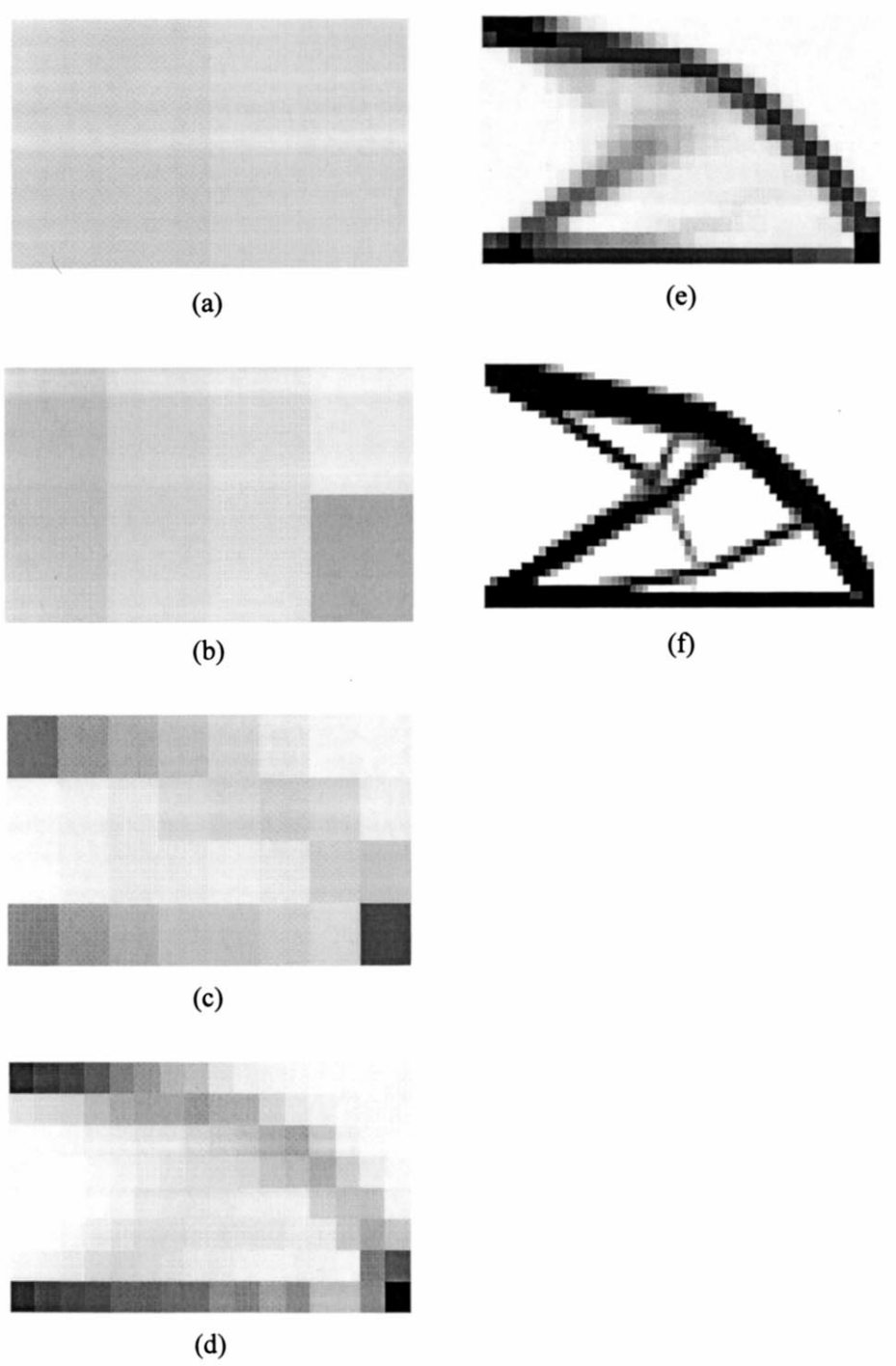

Fig. 18. MTOP started at Resolution Level 3. The results are obtained at (a) Level 6 ($N_{\text{iter}} = 6$, $N_f = 15$, $L_{\text{opt}} = 13946.88$), (b) Level 5 ($N_{\text{iter}} = 3$, $N_f = 11$, $L = 11501.65$), (c) Level 4 ($N_{\text{iter}} = 7$, $N_f = 21$, $L_{\text{opt}} = 7709.19$), (d) Level 3 ($N_{\text{iter}} = 3$, $N_f = 11$, $L_{\text{opt}} = 6309.56$), (e) Level 2 ($N_{\text{iter=13}}$, $N_f = 39$, $L_{\text{opt=4792.8}}$), (f) Level 1 (N_{iter}, $N_f = 111$, $L_{\text{opt=3874.0}}$).

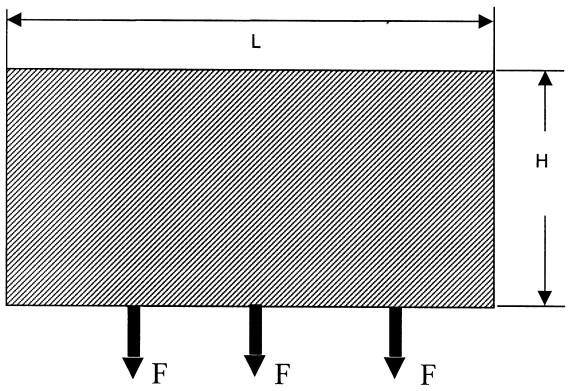

Fig. 19. A compliance minimization problem under 3 point loads (L = 200, H = 100).

1. The final optimal result of Fig. 13(f) is topologically simpler than the results obtained by FTOP or the direct-density based optimization. Compare Figs. 10(b) and 13(f). Furthermore, the objective function appears to reach the minimum value. Compare Tables 3 and 5.
2. Furthermore, intermediate density values virtually disappear in the final configuration shown in Fig. 13(f).
3. No remeshing is required as the degree of resolution improves. Only the final finest discretization is needed in MTOP.

Among others, the fact that a topologically simpler structure can be obtained is striking. To find such a simple structure, an additional constraint such as the perimeter constraint (see Sigmund and Petersson, 1998) has to be imposed explicitly. However, the present MTOP even without any explicit constraint yields a topologically simple structure while meeting the design objective of minimum compliance. Furthermore, MTOP also tends to push the objective function to take the global minimum value.

Though intermediate density values do not appear in the final configuration, the total number of iterations is quite large (see Table 5). The same convergence criteria ($C_a = C_r = 0.001$) are used for all levels. To improve the solution convergence rate, we may start with a higher resolution level. This is motivated by the observation that the optimized results at too coarse resolution levels such as Resolution 6 and Resolution 7 may be far from the final results. Fig. 14 shows the results by MTOP started at Resolution Level 3. The post-processed configuration shown in Fig. 14(d) is virtually identical to the one shown in Fig. 13(f). The iteration numbers and the object function values are tabulated in Table 6. The total numbers of iterations and function evaluations have been reduced substantially though somewhat relaxed convergence criteria are used.

As the next problem, the optimization depicted in Fig. 15 is considered. Since either the Haar wavelet-based FTOP or MTOP always gives improved results, we do not repeat the direct density-based optimization. Fig. 16 shows the optimized result by FTOP where Figs. 17 and 18 show the results by MTOP started at Levels 3 and 6, respectively. It is clear that the optimized configurations in Fig. 18 by MTOP are less complex than the configuration by FTOP. The optimized configurations by FTOP and MTOP started at Level 3 are the same as the existing result (see Rozvany et al., 1995; Diaz and Bensøe, 1992). However, FTOP started at Level 6 gives a different configuration from those by FTOP or MTOP started at Level 3. Furthermore, the corresponding value of the object function is smaller than the others. Since optimization is carried out progressively throughout all resolution levels, the present result tends to approach the global minimum. Though more theoretical investigations on this aspect need to be carried out, this property of MTOP is very useful in practical optimization problems.

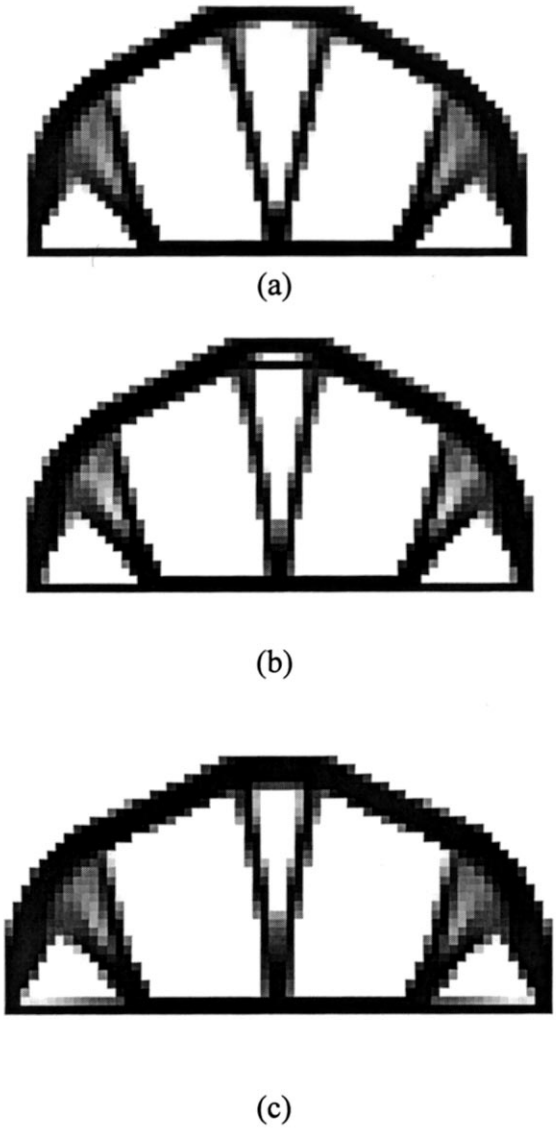

Fig. 20. The results (a) by FTOP, (b) by MTOP started at Level 3 and (c) by MTOP started at Level 6 without post-processing.

Finally, the compliance minimization problem defined in Fig. 19 is considered. The results by FTOP and MTOP started at Levels 3 and 6 are compared in Fig. 20. Only the final results by MTOP are shown in Fig. 20. All the results have the same topology complexity, but a slightly better result (in terms of intermediate density values) is obtained by MTOP started at Level 6.

6. Conclusions

A new concept of multi-resolution multi-scale topology optimization (MTOP) is presented in this

work. The wavelets are used as the framework for multi-resolution multi-scale topology optimization (MTOP) and the underlying wavelet theories are briefly given. The removal of the side constraints imposed on the original density has resulted in the successful numerical implementation of MTOP. Among others, it is found that MTOP yields globally optimal structures having as simple topologies as possible. The present MTOP formulation did not use any explicit constraint such as a perimeter constraint in obtaining such structures. Considering the striking results, it is believed that multi-resolution multi-scale topology optimization will open a new paradigm for topology optimization. Obviously, this new topology optimization approach should be accompanied by more theoretical foundations.

References

Bendsøe, M.P., 1995. Optimization of Structural Topology, Shape and Material. Springer, New York.

Bendsøe, M.P., Kikuchi, N., 1988. Generating optimal topologies in structural design using a homogenization method. Comp. Meth. Appl. Mechs. Engng 71, 197–224.

Choi, K.W., 1999. A study on the topology optimization using the wavelet transform. Master's thesis, Seoul National University, Seoul, Korea.

Chui, C.K., 1992. An Introduction to Wavelets. Academic Press, New York.

Cohen, A., Daubechies, I., Feauveau, J.C., 1992. Biorthogonal bases of compactly supported wavelets. Commun. on Pure and Appl. Math 45, 485–560.

Daubechies, I., 1988. Orthonormal bases of compactly supported wavelets. Commun. on Pure and Appl. Math 41, 909–996.

Daubechies, I., 1992. Ten Lectures on Wavelets. SIAM, Philadelphia, PA.

Diaz, A.R., Bensøe, M.P., 1992. Shape optimization of structures for multiple loading conditions using a homogenization method. Struct. Optim 4, 17–22.

Haar, A., 1910. Zur theorie der orthogonalen funktionensysteme. Math. Annal 69, 331–371.

Harber, R.B., Jog, C.S., Bensoe, M.P., 1996. A new approach to variable-topology shape design using a constraint on perimeter. Struct. Optim 11, 1–12.

Hassani, B., Hinton, E., 1998a. A review of homogenization and topology optimization I — homogenization theory for media with periodic structure. Comput. Struct 69, 707–717.

Hassani, B., Hinton, E., 1998b. A review of homogenization and topology optimization II — analytical and numerical solution of homogenization equations. Comput. Struct 69, 719–738.

Hassani, B., Hinton, E., 1998c. A review of homogenization and topology optimization III — topology optimization using optimality criteria. Comput. Struct 69, 739–756.

Kim, Y.Y., Choi, K.W., 1998. A study on the topology optimization using the wavelet transform. In: 98 Simposium of the Mechanical Design Department, Seoul National University, Seoul, Korea, December 12, 83–91.

Kim, Y.Y., Kim, T.S., 2000. Topology optimization of beam cross section. Int. J. Solids and Struct. 37, 477–493.

Kim, Y.Y., Kim, T.S., 1999. Checkerboard control using the wavelet transform in topology optimization. IDEALAB Report No. 99-1, School of Mechanical Aerospace Engineering, Seoul National University, Seoul, Korea.

Mallat, S., 1989. Multiresolution approximations and wavelet orthonormal bases of $L^2(\mathbf{R})$. Trans. Amer. Math. Soc 315, 69–87.

Mallat, S., 1998. A Wavelet Tour of Signal Processing. Academic Press, New York.

Meyer, Y., 1992. Wavelets and Operators. Advanced Mathematics. Cambridge University Press, Oxford.

Poulsen, T.A., 1999. Multi-scale representations in design optimization. In: Short Paper Proceedings, World Congress of Structural and Multidisciplinary Optimization, Buffalo, New York, May 17–21, 129–131.

Rozvany, G., Bensoe, M.P., Kirsch, U., 1995. Layout optimization of structures. Appl. Mech. Rev 48 (2), 41–108.

Sigmund, O., 1994. Design of material structures using topology optimization. Ph.D. Thesis, Department of Solid Mechanics, Technical University of Denmark.

Sigmund, O., 1997. On the design of compliant mechanisms using topology optimization. Mech. Struct. Mach 25, 495–526.

Sigmund, O., Petersson, J., 1998. Numerical instabilities in topology optimization: A survey on procedures dealing with checkerboards, mesh-dependencies and local minima. Struct. Optim 16, 68–75.

Strang, G., Nguyen, T., 1996. Wavelets and Filter Banks. Cambridge Press, Boston.

Vanderplaats, G.N., 1984a. Numerical Optimization Techniques for Engineering Design. McGraw-Hill, New York.

Vanderplaats, G.N., 1984b. ADS — A Fortran Program for Automated Design Synthesis NASA CR 172460.

Vetterli, M., Kovacevic, J., 1995. Wavelets and Subband Coding. Prentice-Hall, Englewood Cliffs. NJ.